(Online) ISSN 2303-4521
**Periodicals of Engineering and Natural Sciences** *Original Research*
Vol. 14, No. 2, April 2026, pp.103-114

# Computational probe of current responses derived from mass-transport through interconnected pore structures in 3D-printed milli fluidic devices with channel band electrodes

**Jesús E. Contreras-Naranjo [1*], A. D. Rincon-Quintero [1,2], C. L. Sandoval-Rodriguez [1,2], Mauricio Ruiz-Ochoa[1], Omar Lengerke [1], German Bautista-Obregon [1]**
[1] Unidades Tecnológicas de Santander (UTS), Bucaramanga, 680005, Colombia
[2] Universidad del País Vasco UPV/EHU, Spain

*Corresponding author E-mail: jjesuseduardocontrerasnaranj@correo.uts.edu.co

## ABSTRACT

This computational study investigates steady-state current responses in Fused Deposition Modeling (FDM) 3D-printed milli fluidic devices with channel band electrodes under laminar flow conditions. While conventional microfluidic devices are well-characterized using Levich and Thin Layer analytical models, 3D-printed platforms exhibit inherent porosity creating complex current behavior inadequately described by Levich and Thin Layer equations alone. After a mesh convergence study determined appropriate mesh conditions, four device designs considering porous network structure and pore proximity to the electrode were computationally probed. Analysis of these simulations incorporated design and hydrodynamic dimensionless parameters to characterize mass-transport regimes. Previously reported General and Transition analytical models as well as Levich and Thin Layer models were applied for current prediction and mass-transport analysis. As a result, the highest and lowest currents were obtained for a pore continuous to the electrode and a complex pore network structure, respectively. Velocity and concentration profiles reveal that interconnected pore structures and pore – electrode proximity create regions where diffusion, convection, or both transport regimes predominate simultaneously in the same device configuration. While general and transition mass-transport models accurately characterize designs with simpler porous network structures, they diverge under the structural mass-transport constraints of a design with a more complex porous network structure; this identifies critical limitations for existing theory and underscores the need for future framework refinements. Progress in this direction is essential to optimize device design and improve analytical performance in electrochemical sensing applications that employ FDM 3D-printed milli fluidic devices.

**Keywords**: 3D-printed milli fluidic electrochemical devices, simulations, porous network structure, pore proximity, mass-transport regimes

## 1. Introduction

Millimeter-scale platforms such as Fused Deposition Modeling (FDM) 3D-printed milli fluidic devices with channel band electrodes hold considerable promise in analytical chemistry, offering flexibility to either operate as separate analytical platforms or augment established methodologies (for instance, chromatography) [1]–[3]. However, these devices present unique structural features that distinguish them from their conventionally manufactured counterparts [4]–[7]. 3D-printed milli fluidic devices with channel band electrodes inherently contain porous structures distributed throughout their volume, mostly in internal and top layers, which affect both the physical quality and electrical conductivity properties of the fabricated components. These high levels of porosity (10% - 32%) create interconnected microchannels that alter the mass-transport of electroactive species, which can significantly influence their current limiting response [8]–[10]. As a result, different mass-transport regimes can potentially occur at the same time within a single device, creating complex electrochemical behavior that is not adequately described by existing theoretical frameworks developed for non-porous microfluidic systems [11], [12].

On the other hand, the theoretical and computational understanding of mass-transport in traditional micrometer-scale platforms such as microfluidic devices with channel band electrodes has been extensively developed [13], [14]. Finite element simulations and theoretical analysis have been used to successfully characterize the various convection-diffusion zones governed by mass-transport dynamics in single-band microelectrodes and microelectrodes arrays [15]–[17]. Specific circumstances leading to transient, quasi-steady-state, and convective regimes in microfluidic systems have been systematically explored, accounting for the combined effects of device geometry and flow velocity under laminar conditions [18]–[22]. These studies have established fundamental equations such as the Levich equation for convection-dominated regimes and Thin Layer models for diffusion-dominated transport. Despite these advances in modeling microfluidic electrochemical systems, there exists a critical knowledge gap regarding the behavior of current response in millimeter-scale 3D-printed milli fluidic devices with channel band electrodes operating under laminar flow and steady state conditions. Initial approaches have recently emerged aimed at understanding the behavior of these systems [12].

However, the steady-state current responses governed by mass-transport as a function of the porous network structure and proximity of the pore to the electrode in 3D-printed milli fluidic devices with channel band electrodes have not been previously reported in literature. This gap stems from the inherent complexity of integrating numerous parameters such as device geometry, fabrication-dependent porosity, electrode shape, and hydrodynamic flowing conditions, making this extremely difficult to replicate experimentally [5], [8], [12].

The present study is aimed at understanding the steady-state current responses in 3D-printed milli fluidic devices with channel band electrodes considering porous network structure and proximity of the pore to the electrode as a function of design and hydrodynamic parameters under laminar flow conditions. After a mesh convergence study determined appropriate mesh conditions for the computational mass-transport study, four different device designs considering porous structure and proximity of the pore to the electrode were proposed and investigated. Current values extracted from simulations showed that the highest and lowest currents are obtained for a pore continuous to the electrode (design 3) and a complex pore network structure (design 4), respectively. In addition, from velocity and concentration profiles it was evident that pore connectivity and proximity to the electrode can restrict species passage in complex ways, creating regions where diffusion, convection, or both transport mechanisms prevail simultaneously within the same device. While previously reported mass-transport models such as General and Transition models have proven reliable for predicting steady-state current in various porous electrochemical architectures—exemplified here by designs 2 and 3—their predictive accuracy is challenged by the structural complexities of more restrictive geometries, such as design 4. This study identifies these limitations, suggesting that while a full refinement of such frameworks remains beyond our current scope, addressing these specific transport constraints is essential for the future evolution of the field. By elucidating the fundamental relationships between structural features and current electrochemical response, these insights provide essential guidelines for developing more efficient 3D-printed milli fluidic platforms with optimized analytical performance in electrochemical sensing applications.

## 2. Research method

### 2.1 Theoretical framework

The electrochemical response of 3D-printed milli fluidic devices with channel band electrodes is governed by mass-transport phenomena that determine the steady-state limiting current under convective, diffusive, and transition conditions. The following analytical models were employed to describe and predict the current response as a function of device geometry and hydrodynamic parameters [11], [12].
Mass-transport of a reversible redox species A undergoing $n$e$^-$ electron transfer at the electrode surface to yield product B is described by the convection–diffusion equation under steady-state laminar flow:

$$\frac{\partial c}{\partial t} = D\left(\frac{\partial^2 c}{\partial x^2} + \frac{\partial^2 c}{\partial y^2}\right) - u_x(y)\frac{\partial c}{\partial x} \qquad (1)$$

where $D$ is the diffusion coefficient, $c$ is the local species concentration, and $u_x(y)$ is the fully developed parabolic velocity profile across the channel height $h$:

$$u_x(y) = 6u_{av}\frac{y}{h}\left(1 - \frac{y}{h}\right) \qquad (2)$$

where $u_{av}$ is the mean flow velocity.

Three dimensionless groups characterize the system: the geometric ratio $W = w/h$; the Peclet number $Pe = u_{av}h/D$; and the dimensionless current $\psi = i/(nFLDc^0)$, where $w$ is the band electrode width, $n$ is the number of electrons transferred, $F$ is the Faraday constant, and $c^o$ is the upstream bulk concentration.
When convective transport dominates at high $Pe$ (Zone III), the steady-state limiting current at a flat inlaid channel band electrode is given by the Levich equation [11], [12]:

$$i_{Levich} = 0.925nFLc^0(wD)^{2/3}\left(\frac{4u_{av}}{h}\right)^{1/3} \quad (3)$$

Its dimensionless form is:

$$\psi_{Levich} = 1.468nW^{2/3}Pe^{1/3} \quad (4)$$

The diffusion-convection layer thickness is smaller than $h$ and is partially controlled by $w$, rendering $\psi_{Levich}$ a function of $W$. At low $Pe$, the diffusion layer spans the full channel height, and the system operates under Thin Layer conditions (Zone I). The steady-state limiting current is [11], [12]:

$$i_{thin\ layer} = nFc^0u_{av}Lh \quad (5)$$

In dimensionless form:

$$\psi_{thin\ layer} = Pe \quad (6)$$

Because the concentration gradient extends across the entire channel height, $\psi$ is independent of $W$ and is governed solely by the advective flux of analyte entering the electrode region.
In porous FDM-fabricated milli fluidic devices, inherent porosity generates secondary microchannels beneath the electrode that can sustain different mass-transport regimes simultaneously within the same device. Neither the Levich nor the Thin Layer model alone captures the current behavior of the intermediate transition regime (Zone II), where both convection and diffusion contribute to mass-transport. A General analytical model was therefore developed by fitting the following expression to finite-element simulation data spanning all three transport zones [12]:

$$\Psi_{General} = \frac{1.468 \cdot AW^{\frac{2}{3}}Pe^{\frac{1}{3}}\left(\frac{W}{Pe}\right)^C}{B+A\left(\frac{W}{Pe}\right)^C} \quad (7)$$

where A = −0.3268, B = −0.2458, and C = −0.8432 are empirical constants. To obtain higher accuracy within the mixed convection-diffusion regime ($-1.3 \le \log_{10}(W/Pe) \le 0.3$), (7) was refitted exclusively to simulation data in Zone II, yielding the Transition-specific model:

$$\Psi_{Transition} = \frac{1.468 \cdot AW^{\frac{2}{3}}Pe^{\frac{1}{3}}\left(\frac{W}{Pe}\right)^C}{B+A\left(\frac{W}{Pe}\right)^C} \quad (8)$$

where A = −2.9824, B = −1.7920, and C = −1.1939.
When predicting currents within zone II, the transition model outperforms the General model, and both Transition and General models outperform the Levich and Thin Layer models. Together, (7) and (8) constitute a complete analytical framework for predicting and normalizing the limiting current response across all mass-transport regimes in channel band electrodes, applicable to milli fluidic and microfluidic systems alike. Therefore, the mass-transport regime boundaries are Zone III (convection-dominated) for $\log_{10}(W/Pe) < -1.3$; Zone I (diffusion-dominated) for $\log_{10}(W/Pe) > 0.3$; and Zone II (transition) for $-1.3 \le \log_{10}(W/Pe) \le 0.3$ [12].

### 2.2 Computational methods

COMSOL Multiphysics 5.3a (COMSOL AB, Stockholm, Sweden) was used to perform the simulations in this work. The model configuration and its constitutive parameters were previously described and validated in reference [12]. Current curves were obtained from simulations within a potential window of −0.4 V to +0.6 V

using a 10 mV step. The physicochemical parameters for the $[Fe(CN)6]^{4-/3-}$ redox probe were defined as $n = 1$, $F = 96{,}485$ C mol$^{-1}$, $c^0 = 4 \times 10^{-6}$ mol cm$^{-3}$, and $D = 6.39 \times 10^{-6}$ cm$^2$ s$^{-1}$. Limiting currents were measured at +0.6 V as a function of dimensionless design parameter $W$ defined as $w/h$ and the Peclet number $Pe$ under static ($Pe = 0$) and dynamic conditions: low flow rates ($Pe = 100$ and 500) and high flow rates ($Pe = 1000$ and 10000) set at the entrance of the device. Methodology to evaluate limiting currents is well-described in reference [12].

### 2.3 Computational design models to study mass-transport

To study diffusion, convection, and transition mass-transport regimes considering the proximity of the pore to the electrode and the porous network structure in millimeter-scale flow systems such as 3D-printed milli fluidic devices with channel band electrodes, four different designs were proposed. Design 1 evaluates mass-transport in milli fluidic devices with no porosity as shown in Figure 1A. Designs 2 and 3 (Figures 1B and 1C) evaluate the proximity of the pore to the electrode, meanwhile, design 4 (Figure 1D) evaluates the porous network structure in milli fluidic devices.

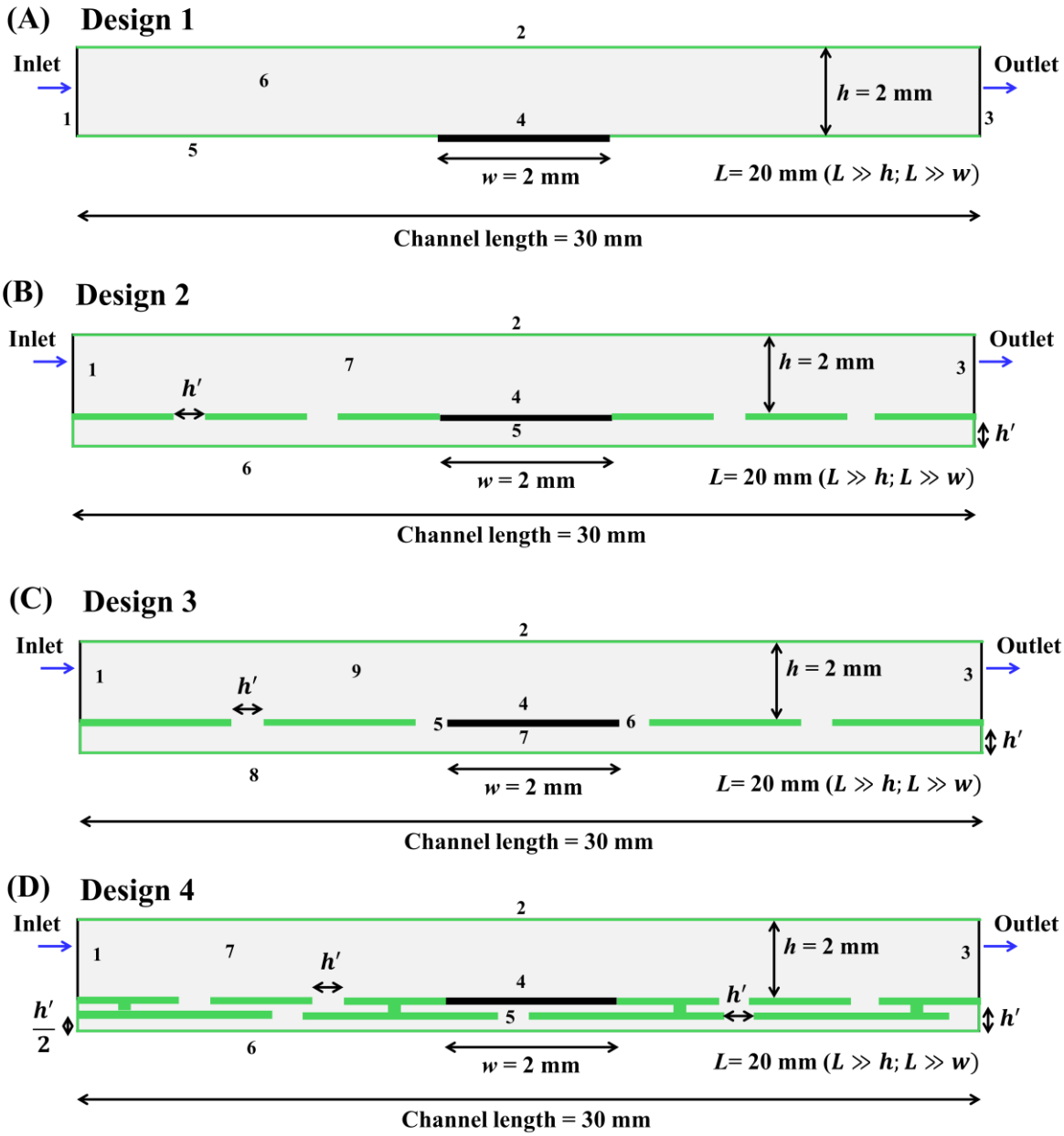


Figure 1. (A) Design 1 is inspired by a traditional microfluidic device with a channel band microelectrode, but here the design is presented at a millimeter-scale. To study the proximity of the pore to the electrode and the porous network structure in the mass-transport through interconnected pore structures in 3D-printed milli fluidic devices with a channel band electrode, designs 2 (B), 3 (C), and 4 (D) were proposed respectively. Boundaries 5 and 6 in design 3 representing the lateral surfaces of the electrode are insulated boundaries where no

electrochemical reaction occurs. In Figures 1B, 1C, and 1D, the models have two channels: the top one (above the electrode) represents the principal channel (channel height *h*) and the bottom one (below the electrode) is a secondary channel (channel height *h'*) used to represent porosity. Both channels are connected by 4 vertical channels of the same width *h'* simulating 10% porosity. The values of *h'* were calculated as reported previously [12]. Designs 2 and 3 have two channels near and next to the electrode, respectively, and the other two channels are distributed symmetrically along the milli fluidic channel. Design 4 has two secondary channels connected by vertical channels of width *h'*. Each secondary channel has a channel height of *h'*/2.

Figure 1 establishes the following dimensional parameters: a channel height of $h$ = 2 mm, a band electrode width $w$ = 2 mm, and a characteristic length $L$ = 20 mm that simultaneously defines the band electrode length and the channel width. The design conditions $L>>h$ and $L>>w$ enables a reduction of a 3D – problem to a 2D-framework. In Figures 1B, 1C, and 1D, the height of the secondary channel (*h'*) also reflects the porosity of the device, which was set as 10% (*h'*= 750 μm). The meshing parameters adopted in the mass-transport simulations were selected from the mesh convergence study. Supplementary Tables S1 – S4 illustrate comprehensive details (boundary conditions, physics, and constitutive equations) employed in mass-transport modelling of device designs 1 – 4, respectively.

### 2.4 Mesh convergence study

To establish the appropriate mesh conditions for the numerical simulation of the millimeter-scale flow system represented in Figure 1D, multiple mesh configurations were constructed by adjusting mesh-defining parameters to yield progressively refined meshes as done previously and shown in Table 1 [12]. The entire model geometry was discretized using a customized general mesh, meanwhile, a customized free triangular mesh was used on the electrode domain. Supplementary Table S4 illustrates comprehensive details (boundary conditions, physics, and constitutive equations) used in the mesh convergence study.

Table 1. Mesh conditions implemented for the simulation of a millimeter-scale flow-system

| General mesh | | | | | |
|---|---|---|---|---|---|
| Mesh | Maximum element size, μm | Minimum element size, μm | Maximum elements growth rate | Curvature factor | Resolution of narrow regions |
| Default | 2010 | 9 | 1.3 | 0.3 | 1 |
| 1 | 300 | 0.6 | 1 | 0.3 | 1 |
| 2 | 30 | 0.6 | 1 | 0.03 | 1 |
| 3 | 20 | 0.6 | 1 | 0.02 | 1 |

| Electrode domain mesh: free triangular | | | | | |
|---|---|---|---|---|---|
| Mesh | Maximum element size, μm | Minimum element size, μm | Maximum element growth rate | Curvature factor | Resolution of narrow regions |
| Default | 2010 | 9 | 1.3 | 0.3 | 1 |
| 1 | 300 | 0.6 | 1 | 0.3 | 1 |
| 2 | 30 | 0.6 | 1 | 0.03 | 1 |
| 3 | 20 | 0.6 | 1 | 0.02 | 1 |

## 3 Results and discussion

### 3.1 Mesh Convergence Study

In the present computational study, the selection of a suitable mesh is critical to ensure accurate current readings, particularly for higher flow rates (*Pe* = 500, 1000, and 10000). Convergence in the limiting currents was achieved between meshes #2 (gray curve) and 3 (yellow curve), which overlapped one another for all evaluated *Pe* (see Figures 2A – E). Table 2 describes the computational time and number of elements for the various meshes considered, and he current values from the different meshes evaluated for 10% porosity are shown in Table 3. The convergence error in the current readings reported in Table 3 was calculated as follows:

$$\text{Convergence error for mesh k (\%)} = \frac{\text{Current for mesh (k)} - \text{Current for mesh (k + 1)}}{\text{Current for mesh (k + 1)}} \times 100$$

where mesh k + 1 is a more refined mesh than mesh k.

From Figure 2 and Tables 2 and 3, mesh #2 was chosen for the following mass-transport computational studies since it presented the best relation between computational time consumed and convergence error among the studied meshes. Therefore, the values of the current readings in all designs under static (*Pe* = 0) and dynamic conditions (*Pe* = 100, 500, 1000, and 10000) for a porosity of 10% are expected to have convergence errors of less than 1.1%.

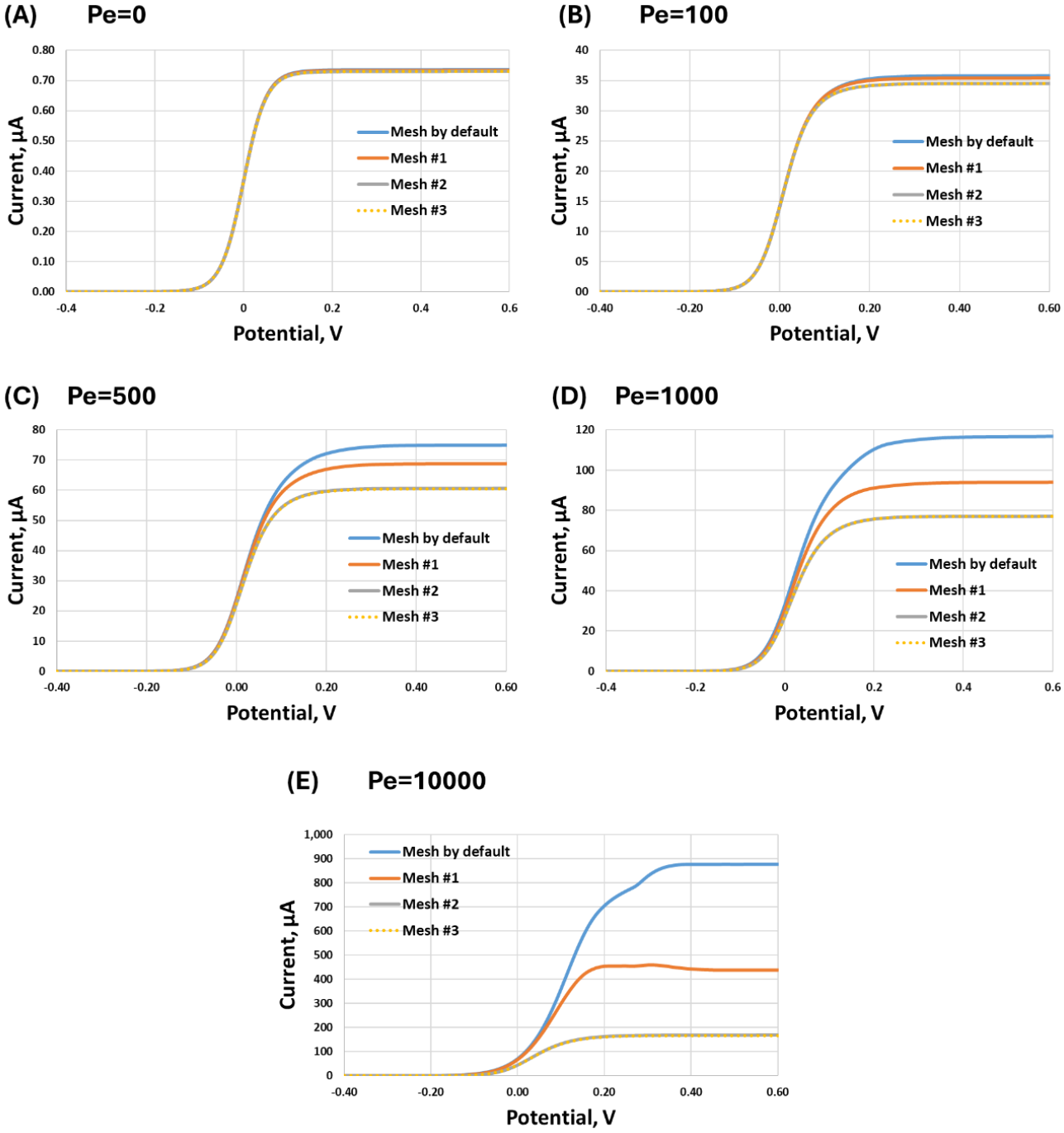


Figure 2. Linear sweep voltammetry simulated and generated from device design depicted in Figure 1D for the different meshes evaluated: mesh by default (blue curve), mesh #1 (orange curve), mesh #2 (gray curve), and mesh #3 (dotted yellow curve) overlapped with mesh #2 at (A) *Pe* = 0, (B) *Pe* = 100, (C) *Pe* = 500, (D) *Pe* = 1000, and (E) *Pe* = 10000.

Table 2. Computational time and number of elements from the different meshes evaluated

| Mesh | Computational Time | # of Elements |
|---|---|---|
| Default | 5 min 20 s | 1563 |
| 1 | 14 min 35 s | 4300 |
| 2 | 15 h 15 min 12 s | 258304 |
| 3 | 29 h 18 min 21 s | 574127 |

Table 3. Simulated current responses and numerical errors across the various meshes evaluated for 10% porosity at *Pe*= 0, 100, 500, 1000, and 10000

| Mesh | No flux | | *Pe* = 100 | | *Pe* = 500 | | *Pe* = 1000 | | *Pe* = 10000 | |
|---|---|---|---|---|---|---|---|---|---|---|
| | Current (μA) | Error (%) | Current (μA) | Error (%) | Current (μA) | Error (%) | Current (μA) | Error (%) | Current (μA) | Error (%) |
| Default | 0.736 | 0.14 | 35.77 | 0.96 | 74.83 | 8.72 | 116.31 | 24.09 | 876.69 | 97.48 |
| 1 | 0.735 | 0.82 | 35.43 | 2.73 | 68.83 | 13.71 | 93.73 | 21.52 | 443.94 | 163.37 |
| 2 | 0.729 | 0.00 | 34.49 | 0.06 | 60.53 | 0.07 | 77.13 | 0.10 | 168.56 | 1.07 |
| 3 | 0.729 | - | 34.47 | - | 60.49 | - | 77.05 | - | 166.78 | - |

### 3.2 Qualitative mass-transport analysis in interconnected pore structures

Once the mesh parameters were chosen, mass-transport through interconnected pore structures in 3D-printed milli fluidic devices with channel band electrodes was evaluated. Figure 3 shows the velocity profiles developed in the different designs evaluated at *Pe* = 10000 and *W* = 1 under steady-state and laminar flow conditions.

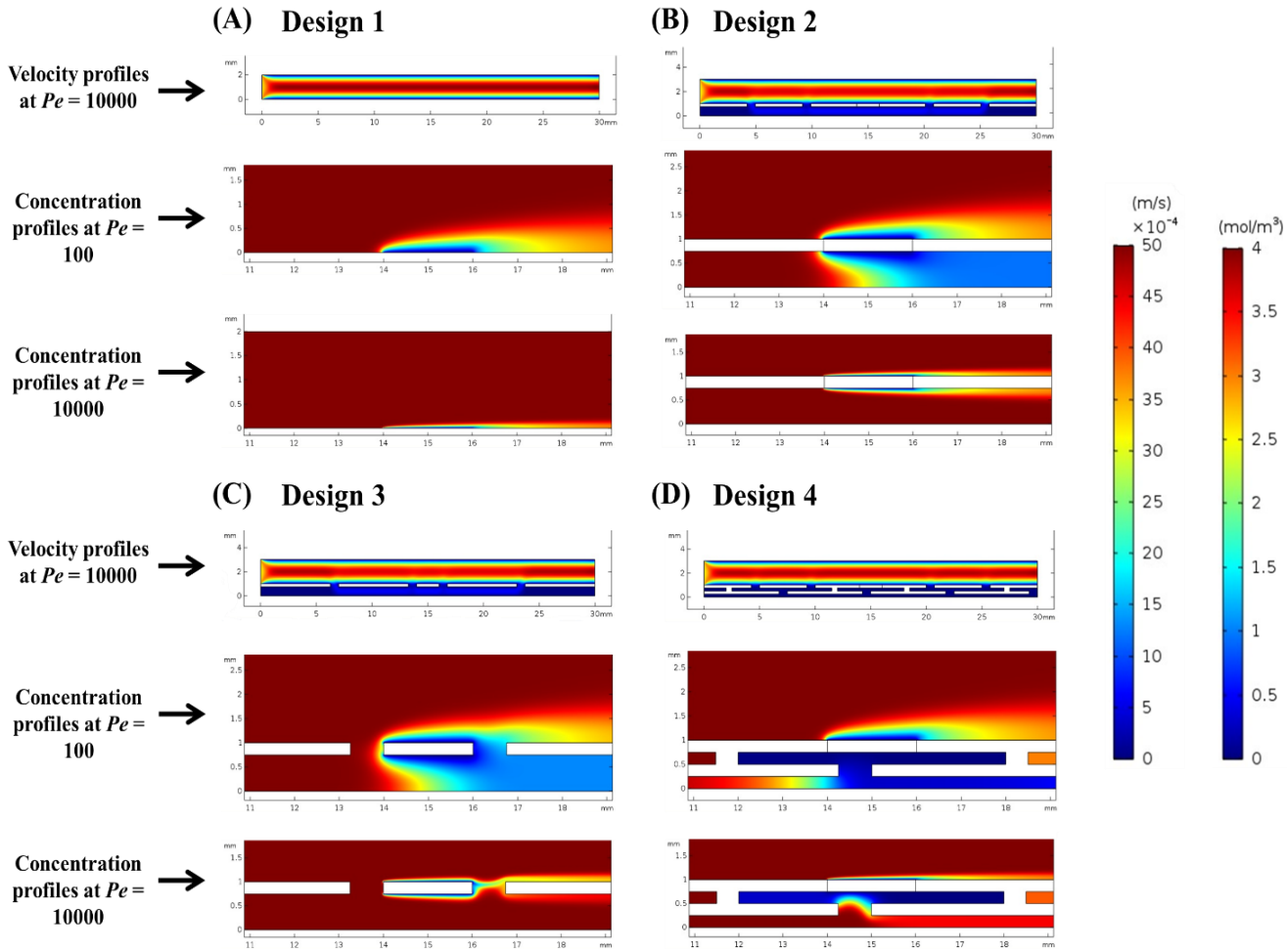


Figure 3. Velocity (full simulation domain) and concentration profiles (zoomed in around the electrode surface) developed in the different designs evaluated (A) design 1, (B) design 2, (C) design 3, and (D) design 4 at *Pe* = 100 and 10000 and *W* = 1 under steady-state and laminar flow conditions.

As it can be observed in Figure 3, the porous network structure and proximity of the pore to the electrode affects the flux of species entering the principal channel, causing a fraction of the flow to be redirected beneath it, thus promoting the formation of distinct mass-transport zones such as convection, diffusion, or both.

To qualitatively study the current response governed by mass-transport regimes as a function of the porous network structure and the proximity of the pore to the electrode, concentration profiles of the redox species were analyzed from steady-state and laminar flow simulations. Figure 3 presents magnified views of the electrode vicinity, illustrating the concentration profiles within the millimeter-scale device designs at *Pe* = 100 and *Pe* = 10000. Figure 3 shows that at *Pe* = 100, the convective regime prevails in the principal channel across all device designs, whereas transition regime predominates in the secondary channel of the designs 2 and 3. This transition regime is characterized by a current primarily dictated by diffusion transport, closely approximating the Thin Layer regime while still presenting a perceptible divergence from it. In this scenario, the convective-diffusion layer reaches the channel ceiling and undergoes lateral expansion via diffusion against the flow resembling the characteristic behavior that is observed in the complete Thin Layer diffusional regime [11], [12]. At *Pe* = 10000, the convective regime prevails in the principal and secondary channels, above and below the electrode for device designs 1 – 3. Similarly, from designs 2 and 3, it can be observed that the proximity of the pore to the electrode does not have a significant influence on the mass-transport regimes developing above and below the electrode.

In addition, Figure 3D reveals the presence of stagnation zones in design 4, in the region beneath the electrode, as a product of the flow restriction imposed by the porous network structure and the absence of pores continuous with the electrode. From Figure 3D, the convective regime predominates in the principal channel for all *Pe* evaluated; meanwhile, diffusion prevails in the secondary channel at *Pe* = 100. In addition, a more complex mass-transport regime not easily characterized as diffusion, convection, or transition develops progressively as *Pe* increases from 500 to 10000 (see Figure 3D and Supplementary Figure S2). The complete set of simulation images of the velocity and concentration profiles at different *Pe* (0, 100, 500, 1000, and 10000) can be seen in Supplementary Figures S1 and S2.

### 3.3 Quantitative mass-transport and current response analysis in interconnected pore structures

For the quantitative analysis, total current limiting responses coming from the upper and lower surfaces of the electrode were measured for each corresponding device design as a function of the porous network structure and proximity of the pore to the electrode at the different *Pe* evaluated. For design 3, the lateral surfaces of the electrode are insulated boundaries where no electrochemical reaction occurs. Figure 4 shows that the highest current is obtained when the pore is continuous with the electrode (design 3), closely followed by the current generated when the pore is positioned at a distance from the electrode for all *Pe*. Meanwhile the lowest current is observed when a more complex pore network structure (design 4) is considered for all *Pe*.

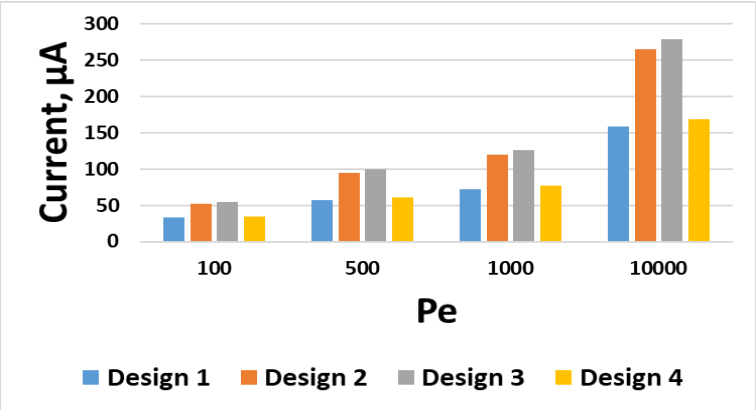


Figure 4. Total limiting current responses coming from the upper and lower surfaces of the electrode for each corresponding device design at the different *Pe* evaluated.

When considering the proximity of the pore to the electrode, a comparative quantitative analysis of the current response as a function of the *Pe* reveals a consistent current response enhancement for design 3 over design 2. Across the evaluated range (*Pe* = 100, 500, 1000, and 10000), design 3 exhibited a relative current increase spanning from 4.71% to 5.42%. Notably, the magnitude of this improvement scales with the convective regime, reaching its peak at *Pe* = 10000. This trend suggests that the structural modifications in design 3, with pores located right next to the electrode, effectively improve mass transport, particularly under high-flow conditions.

On the other hand, when the porous network restricts the flow reaching the electrode from below (design 4), stagnation zones are generated, resulting in a slight increase in current (2.3%, 5.4%, 6.6%, and 6.5% for *Pe* = 100, 500, 1000, and 10000, respectively) relative to the porosity-free system (design 1). This interconnected pore network can create pathways for electroactive species transport that fundamentally alter the electrochemical response compared to milli fluidic non-porous systems. Therefore, the pore connectivity and proximity to the electrode can restrict species passage in complex ways, potentially creating regions where diffusion, convection, or both transport mechanisms prevail simultaneously within the same device.

Now, we compare currents retrieved from simulations (*Pe* = 100, 500, 1000, and 10000) to currents predicted by traditional theoretical models such as Levich and Thin Layer and recently formulated General and Transition models (see Equations 4, 6, 7, and 8, respectively) as a function of *W* and *Pe* for each corresponding device design at 10% porosity (see Figure 5). To calculate *W* and *Pe* at the top and underside faces of the electrode, the flow rate through the principal and secondary channels were obtained from the numerical simulations and the respective channel heights (*h* or *h'*) were employed. The $\log_{10}(W/Pe)$ values which establish the zones for the different mass-transport regimes such as convective, diffusion, and transition developed in each of the device configurations are set in the theoretical framework section and references [11], [12].

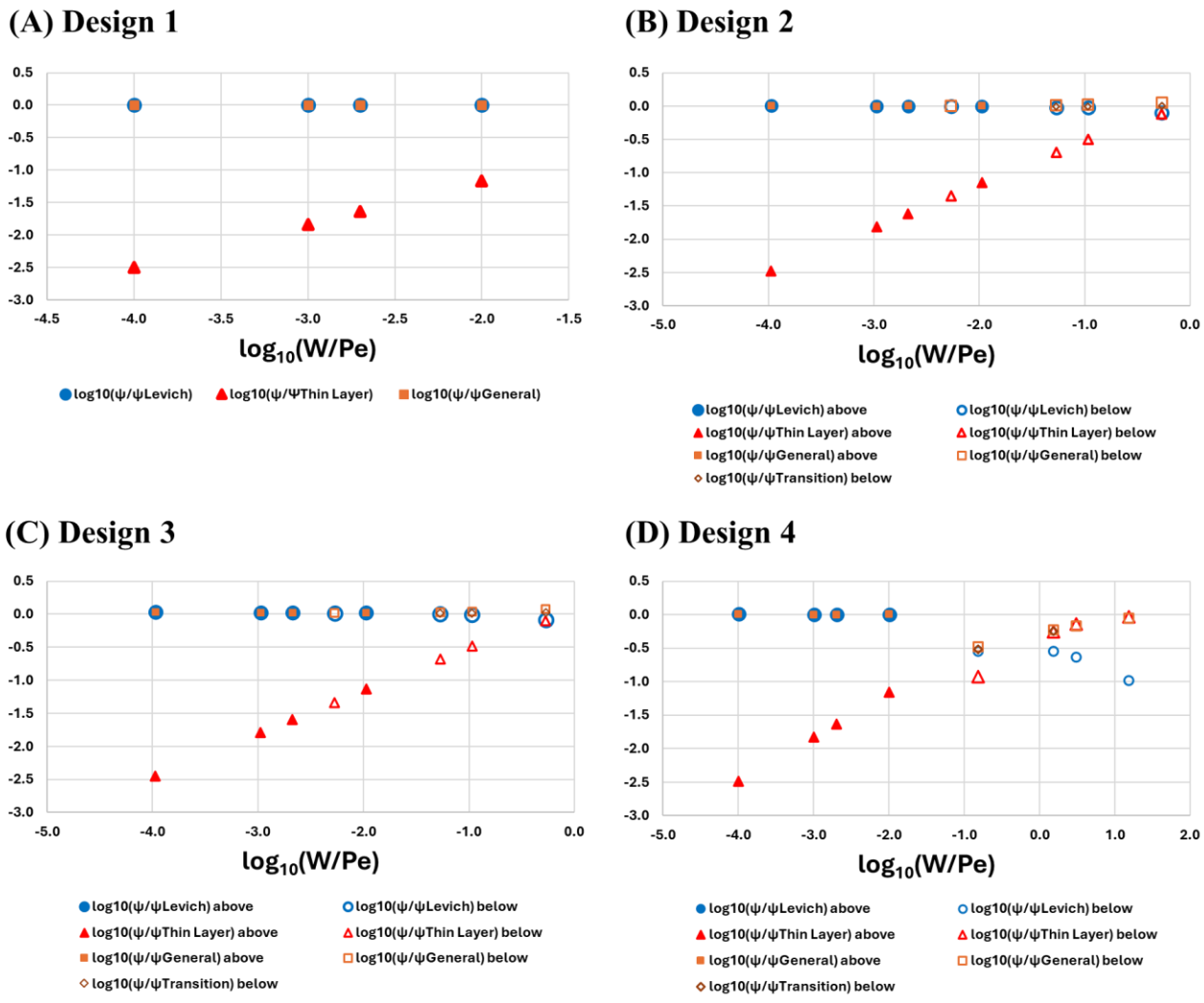


Figure 5. Normalized current variations of $\log_{10}(\Psi/\Psi_{Levich})$ (blue dots), $\log_{10}(\Psi/\Psi_{Thin\ Layer})$ (red triangles), $\log_{10}(\Psi/\Psi_{General})$ (orange squares), and $\log_{10}(\Psi/\Psi_{Transition})$ (green diamonds) versus $\log_{10}(W/Pe)$ extracted from simulations (Figure 3) and generated from (A) design 1, (B) design 2, (C) design 3, and (D) design 4.

From Figure 5, the electrode surface facing the main channel produces currents that are well-predicted and normalized by the Levich ($\log_{10}(\Psi/\Psi_{Levich})$) and the General ($\log_{10}(\Psi/\Psi_{General})$) models in the range of $-4 \leq \log_{10}(W/Pe) \leq -2$, showing values consistently close to zero for all designs of the millimeter-scale fluidic device. This confirms the predominance of the convective regime in the principal channel across all device designs for

all $Pe > 0$ studied. From designs 2 (Figure 5B) and 3 (Figure 5C), currents measured at the electrode surface facing the secondary channel are well-predicted and can be properly normalized by the Transition ($\log_{10}(\Psi/\Psi_{Transition})$) and the General models in the range of $-2.27 \leq \log_{10}(W/Pe) \leq -0.27$, showing values consistently close to zero for both designs. Also, from design 4 (Figure 5D), the electrode surface facing the secondary channel produces a current that is well-predicted and normalized by the Thin Layer and the General models at $\log_{10}(W/Pe) = 1.18$ for the diffusion regime. Meanwhile, the structural constraints within the porous network impede the free flow of species beneath the electrode, inducing a mass-transport regime that diverges from standard diffusion, convection, or transition developed when species flow through a clearly defined channel towards the electrode surface as $Pe$ increases. Consequently, both the general and transition models fail to accurately predict the generated current within the range of $-0.82 \leq \log_{10}(W/Pe) \leq 0.18$. Furthermore, the general model exhibits a specific breakdown in predictive capability at $\log_{10}(W/Pe) = 0.48$. Although the general and transition models remain reliable and effective for predicting steady-state current response in porous electrochemical milli fluidic systems—such as designs 2 and 3 —they exhibit clear limitations when applied to the complex architecture of design 4. Therefore, further research that lies outside the scope of this work is required to refine these theoretical frameworks, enhancing their robustness to encompass the specific transport conditions identified in more constrained geometries.

Then, the zone diagram showing the location of zones I (diffusion regime), II (transition regime), and III (convective regime) for the different device designs was constructed (Figure 6). Previous computational work that only considered a simple porous network structure (similar to design 2) illustrated how current responses in 3D – printed milli fluidic devices with channel band electrodes can be expected to involve more than one transport regime simultaneously [12]. Our work further demonstrates that current behavior is governed by the convective, diffusion, and transition mass – transport regimes, that can occur simultaneously, in a 3D – printed milli fluidic device with a channel band electrode exhibiting more complex porous network structures.

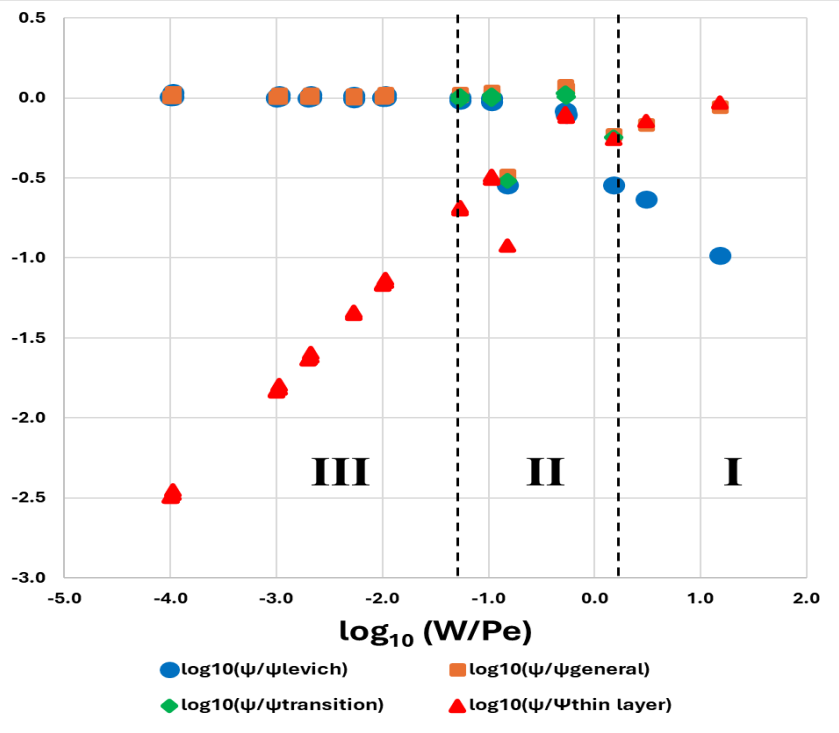


Figure 6. Zone diagram constructed from Figure 5 showing the locations of zones I (diffusion), II (transition), and III (convection). Simulated current variations of $\log_{10}(\Psi/\Psi_{Levich})$ (blue dots), $\log_{10}(\Psi/\Psi_{Thin\ Layer})$ (red triangles), $\log_{10}(\Psi/\Psi_{General})$ (orange squares), and $\log_{10}(\Psi/\Psi_{Transition})$ (green diamonds) versus $\log_{10}(W/Pe)$ extracted from simulations (Figure 3) and generated from each corresponding device design (Figure 1).

## 4 Conclusions

This study enabled a deeper understanding of current behavior considering porous network structure and pore-electrode proximity in 3D-printed milli fluidic devices with channel band electrodes under steady-state laminar flow conditions.

A systematic mesh convergence analysis was performed to establish the numerical reliability of the electrochemical simulations. The study demonstrated that while coarse discretization is sufficient for diffusion-dominated regimes ($Pe = 0$, error < 0.15%), high-convective conditions ($Pe = 10000$) necessitate a significant increase in nodal density to resolve thinning boundary layers. By implementing a refined mesh of over $2.5 \times 10^5$ elements, the relative error was successfully reduced to 1.07%, effectively eliminating grid-dependent artifacts. This rigorous validation ensures that the observed current enhancements are physically grounded, providing a high-fidelity framework for evaluating the performance of the proposed designs across three orders of magnitude of *Pe* number.

Velocity and concentration profiles at different evaluated *Pe* values enabled qualitative identification of simultaneous convection, diffusion, and transition regimes in devices considering porous network structure and pore-electrode proximity as design factors. Currents extracted from simulations determined that the presence of these transport regimes affected the current generated at the electrode. The highest current generated by the electrode was obtained when the pore was continuous to the electrode, while the lowest current was obtained with the most robust porous network structure evaluated.

Convection, diffusion, and transition zones were quantitatively established in each evaluated device design as a function of $\log_{10}(W/Pe)$, as expected from reference [12]. This confirmed the transport regimes qualitatively observed from velocity and concentration profiles in the main and secondary channels of the devices. This study validates the efficacy of general and transition models for standard porous electrochemical systems yet simultaneously identifies critical predictive gaps when applied to more restrictive structural configurations, such as design 4. The limitations observed here define the frontier for next-generation analytical frameworks. Enhancing the robustness of these models to reconcile specialized transport conditions remains a necessary trajectory for future investigation, providing a roadmap for the continued evolution of FDM 3D-printed milli fluidic device design and characterization for electrochemical sensing applications.

## Declaration of competing interest

The authors declare that they have no known financial or non-financial competing interests in any material discussed in this paper.

## Funding information

No funding was received from any financial organization to conduct this research.

## Acknowledgements

The authors express special thanks to the Unidades Tecnológicas de Santander (UTS) for supporting this work.

## Author contribution

Jesús E. Contreras – Naranjo: conceptualization, computational design, data analysis, and manuscript writing. A. D. Rincon-Quintero: contribution to methodological development and support in analytical interpretation. C. L. Sandoval-Rodriguez and Mauricio Ruiz-Ochoa: support in results interpretation and graphical data presentation. Omar Lengerke and German Bautista-Obregon: academic supervision and critical review of methodological consistency. All authors reviewed and approved the final version of the manuscript.

## References

[1] G. D. O'Neil, S. Ahmed, K. Halloran, J. N. Janusz, A. Rodríguez, and I. M. Terrero Rodríguez, "Single-step fabrication of electrochemical flow cells utilizing multi-material 3D printing," *Electrochem. commun.*, vol. 99, pp. 56–60, 2019, doi: https://doi.org/10.1016/j.elecom.2018.12.006.

[2] J. F. Hernández-Rodríguez, D. Rojas, and A. Escarpa, "Print-Pause-Print Fabrication of Tailored Electrochemical Microfluidic Devices," *Anal. Chem.*, vol. 95, no. 51, pp. 18679–18684, 2023, doi: 10.1021/acs.analchem.3c03364.

[3] M. Chávez and A. Escarpa, "3D-Printed Dual-Channel Flow-Through Miniaturized Devices with Dual In-Channel Electrochemical Detection," *Anal. Chem.*, vol. 97, no. 5, pp. 2667–2677, 2025, doi: 10.1021/acs.analchem.4c04099.

[4] E. G. Gordeev, A. S. Galushko, and V. P. Ananikov, "Improvement of quality of 3D printed objects by elimination of microscopic structural defects in fused deposition modeling," *PLoS One*, vol. 13, no. 6,

2018, doi: 10.1371/journal.pone.0198370.
[5] M. Al Khatib *et al.*, "Effect of electrode shape and flow conditions on the electrochemical detection with band microelectrodes," *Sensors (Switzerland)*, vol. 18, no. 10, pp. 31–39, 2018, doi: 10.3390/s18103196.
[6] J. E. Contreras-Naranjo, V. H. Perez-Gonzalez, M. A. Mata-Gómez, and O. Aguilar, "3D-printed hybrid-carbon-based electrodes for electroanalytical sensing applications," *Electrochem. commun.*, vol. 130, p. 107098, 2021, doi: https://doi.org/10.1016/j.elecom.2021.107098.
[7] J. S. Stefano *et al.*, "Electrochemical (Bio)Sensors Enabled by Fused Deposition Modeling-Based 3D Printing: A Guide to Selecting Designs, Printing Parameters, and Post-Treatment Protocols," *Anal. Chem.*, vol. 94, no. 17, pp. 6417–6429, 2022, doi: 10.1021/acs.analchem.1c05523.
[8] Y. Liao *et al.*, "Effect of Porosity and Crystallinity on 3D Printed PLA Properties," *Polymers (Basel).*, vol. 11, no. 1487, pp. 1–14, 2019.
[9] E. M. Richter *et al.*, "Complete Additively Manufactured (3D-Printed) Electrochemical Sensing Platform," *Anal. Chem.*, vol. 91, no. 20, pp. 12844–12851, Oct. 2019, doi: 10.1021/acs.analchem.9b02573.
[10] N. Vidakis, C. David, M. Petousis, D. Sagris, N. Mountakis, and A. Moutsopoulou, "The effect of six key process control parameters on the surface roughness, dimensional accuracy, and porosity in material extrusion 3D printing of polylactic acid: Prediction models and optimization supported by robust design analysis," *Adv. Ind. Manuf. Eng.*, vol. 5, p. 100104, 2022, doi: https://doi.org/10.1016/j.aime.2022.100104.
[11] C. Amatore, N. Da Mota, C. Sella, and L. Thouin, "Theory and Experiments of Transport at Channel Microband Electrodes under Laminar Flows. 1. Steady-State Regimes at a Single Electrode," *Anal. Chem.*, vol. 79, no. 22, pp. 8502–8510, Nov. 2007, doi: 10.1021/ac070971y.
[12] J. E. Contreras-Naranjo, V. H. Perez-Gonzalez, M. A. Mata-Gómez, and O. Aguilar, "Computational and Theoretical Methods for Mass-Transport Analysis in 3D-Printed Milli Fluidic Electrochemical Devices with Channel Band Electrodes," *Chemosensors*, vol. 13, no. 11, 2025, doi: 10.3390/chemosensors13110401.
[13] M. F. Santillo, A. G. Ewing, and M. L. Heien, "Trends in computational simulations of electrochemical processes under hydrodynamic flow in microchannels," *Anal. Bioanal. Chem.*, vol. 399, pp. 183–190, 2011, [Online]. Available: https://api.semanticscholar.org/CorpusID:6175395
[14] R. G. Compton, A. C. Fisher, R. G. Wellington, P. J. Dobson, and P. A. Leigh, "Hydrodynamic voltammetry with microelectrodes: channel microband electrodes; theory and experiment," *J. Phys. Chem.*, vol. 97, no. 40, pp. 10410–10415, Oct. 1993, doi: 10.1021/j100142a024.
[15] C. Amatore, C. Pebay, C. Sella, and L. Thouin, "Mass transport at microband electrodes: transient, quasi-steady-state, and convective regimes.," *Chemphyschem*, vol. 13, no. 6, pp. 1562–1568, Apr. 2012, doi: 10.1002/cphc.201100942.
[16] J. A. Alden and R. G. Compton, "Hydrodynamic voltammetry with channel microband electrodes: axial diffusion effects," *J. Electroanal. Chem.*, vol. 404, no. 1, pp. 27–35, 1996, doi: https://doi.org/10.1016/0022-0728(95)04399-3.
[17] R. G. Compton, R. A. W. Dryfe, J. A. Alden, N. V Rees, P. J. Dobson, and P. A. Leigh, "Hydrodynamic voltammetry with channel microband electrodes: potential step transients," *J. Phys. Chem.*, vol. 98, no. 4, pp. 1270–1275, Jan. 1994, doi: 10.1021/j100055a037.
[18] V. Carvalho, R. O. Rodrigues, R. A. Lima, and S. Teixeira, "Computational simulations in advanced microfluidic devices: A review," *Micromachines*, vol. 12, no. 10, pp. 1–14, 2021, doi: 10.3390/mi12101149.
[19] Y. Ma, C. Sella, T. Delahaye, and L. Thouin, "Highlighting the operating regimes of microchannel electrodes under laminar flow: Mapping of photoluminescence and electrochemiluminescence through semi-transparent electrodes," *Electrochem. commun.*, vol. 165, p. 107759, 2024, doi: https://doi.org/10.1016/j.elecom.2024.107759.
[20] C. Amatore, N. Da Mota, C. Sella, and L. Thouin, "Theory and Experiments of Transport at Channel Microband Electrodes Under Laminar Flow. 3. Electrochemical Detection at Electrode Arrays under Steady State," *Anal. Chem.*, vol. 82, no. 6, pp. 2434–2440, Mar. 2010, doi: 10.1021/ac902788v.
[21] C. Amatore, N. Da Mota, C. Lemmer, C. Pebay, C. Sella, and L. Thouin, "Theory and Experiments of Transport at Channel Microband Electrodes under Laminar Flows. 2. Electrochemical Regimes at Double Microband Assemblies under Steady State," *Anal. Chem.*, vol. 80, no. 24, pp. 9483–9490, Dec. 2008, doi: 10.1021/ac801605v.
[22] C. Amatore, C. Lemmer, C. Sella, and L. Thouin, "Channel Microband Chronoamperometry: From Transient to Steady-State Regimes," *Anal. Chem.*, vol. 83, no. 11, pp. 4170–4177, Jun. 2011, doi: 10.1021/ac2004604.